New synthesis routes and catalytic applications of ferrierite crystals. Part 2: the effect of OSDA type on zeolite properties and catalysis

Enrico Catizzone, Massimo Migliori, Tzonka Mineva, Stijn van Daele, Valentin Valtchev, Girolamo Giordano

New synthesis routes and catalytic applications of ferrierite crystals. Part 2: the effect of OSDA type on zeolite properties and catalysis

Enrico CATIZZONE [a], *Massimo MIGLIORI** [b], *Tzonka MINEVA* [c], *Stijn van DAELE* [d], *Valentin VALTCHEV* [e] *and Girolamo GIORDANO* [b]

[a] ENEA-Italian National Agency for New Technologies, Energy and Sustainable Economic Development, Trisaia Research Centre, I-75026, Rotondela (MT), Italy.

[b]University of Calabria, Department of Environmental and Chemical Engineering, Via P. Bucci – I-87036 Rende (CS), Italy.

[c] Matériaux Avancés pour la Catalyse et al Santé, UMR 5253 CNRS/UM/ENSCM, Institut Charles Gerhardt de Montpellier (ICGM), 240, Avenue du Professeur Emile Jeanbrau, 34296, Montpellier cedex 5, France.

[d] Total Research and Technology Feluy (TRTF), Zone Industrielle C, 7181 Feluy, Belgium.

[e] Laboratoire Catalyse et Spectrochimie CNRS, ENSICAEN, Université de Caen Basse-Normandie, 6 Boulevard Maréchal Juin, Caen, France

*Corrisponding author email : massimo.migliori@unical.it

* Corresponding author
Email: massimo.migliori@unical.it
Telephone: +39 0984496641

ABSTRACT

Tailoring of physicochemical properties of synthetic zeolites is of paramount importance when these materials are applied as heterogenous catalysts. In this work, the effect of the synthesis system and in particular of the organic structure directing agent (OSDA) on acidity, crystal morphology, and catalytic behavior of FER-type materials is studied. FER-type zeolites with similar Si/Al ratio and crystal size range 0.3-15 µm are synthesized by changing OSDA type or by adding surfactant. A crystallization kinetic analysis shows that the stability of the zeolitic phase strongly depends on the OSDA type. In particular, the crystallization time strongly affects the purity of the FER phase when tetrahydrofuran is used as a template. Furthermore, it is found that long amines as 1,8-diaminooctane can play a role of OSDA obtaining highly crystalline FER-type crystals and with a high Lewis acid sites concentration. FT-IR and ^{27}Al-NMR analyses show that all of the synthesized samples possess different Lewis acid sites concentration associated with extra-framework Al-OH species that are not detected by NMR analysis. Catalytic tests in methanol-to-dimethyl ether reaction reveal that synthesized samples exhibit different catalytic behavior. In particular, large (10-15 µm) FER-type catalyst synthesized with tetrahydrofuran suffer deactivation caused by a higher carbon deposit level. On the contrary, nano-sized FER-type crystals, prepared by using pyrrolidine as OSDA and a surfactant, exhibits high selectivity and considerable resistance to coke deposition.

Keywords: Ferrierite zeolite, synthesis, crystal morphology, Brønsted-Lewis acidity, methanol conversion.

1. INTRODUCTION

Activity, selectivity and stability of zeolites catalysts are recognised to depend upon several factors as zeolite structure, crystal size and nature of active sites. Zeolite channel system (channel orientation and opening size) and diffusion pathway are well-known factors affecting the accessibility of the active sites, products distribution and catalyst deactivation [1-5] strongly. Zeolites channel system is also a critical factor that controls the deactivation by coke deposition; thus zeolites with lower channels dimensionality suffer from more rapid deactivation [6].

Nevertheless, zeolites with a similar channel system can exhibit different catalytic behaviour depending on the nature of acid sites. Hence, the acid sites concentration, typology (Brønsted and Lewis), strength, and location are important parameters when zeolites are applied as heterogeneous catalysts [7-13].

Furthermore, catalyst resistance to deactivation as well as catalyst effectiveness can be improved by changing the size and morphology of zeolite crystals [14-16]. In particular, the application of nano-sized or hierarchical zeolite crystals permits to reduce coke formation and enhance the diffusion of reactant species improving catalyst performances [17-19].

Therefore, the ability of zeolite to be modified by both *in situ* and post-synthesis treatments is of considerable importance for the industrial perspective, particularly in the area of heterogenous catalysis [20-23].

Ferrierite (FER) is an important zeolite applied in applied as catalyst in the skeletal isomerization of n-butene for the production of iso-butene and as additive to ZSM-5 catalyst in the dewaxing by selective cracking process for the production of lubricant

[24]. FER framework consists of an intersecting 2-dimensional system of 10- (5.4 x 4.2 Å) and 8- (4.8 x 3.5 Å) member ring channels and can by synthesised with Si/Al ratios ranging from 5 to infinity [25, 26]. The particular channel configuration of FER framework is appropriate for processing small molecules. In particular, FER-type crystals have recently ranked as a reliable acid catalyst for dimethyl ether (DME) production. DME is considered a reliable alternative fuel for Diesel engines thanks to its high cetane number, low ignition-temperature and soot-free exhausted gases [27-31]. Furthermore, DME is an essential intermediate compound in olefins production from methanol [32, 33]. DME can be produced by either double-step or one-step route [31]. Briefly, in the double-step process, methanol is synthesised from syngas over copper-based catalysts, purified and then dehydrated to DME in a separate reactor over an acid catalyst. In one-step process, both synthesis and dehydration of methanol are carried out in a single reactor over a multi-functional metal/acid catalyst. From an economic point of view, one-step process seems to be more profitable. Furthermore, a growing attention is receiving the one-step DME synthesis starting from CO_2-rich syngas or CO_2/H_2 mixture [34]. γ-Al_2O_3 is the most studied catalyst for the methanol dehydration step thanks to the high selectivity towards DME at the typical reaction temperature adopted for both the direct and the indirect routes, inhibiting olefins formation thanks to its low acidity [31]. Although this indisputable advantage, high reaction temperature is necessary (about 300 °C) to promote satisfactory results in terms of methanol conversion. Furthermore, the presence of water molecules formed during the reaction suppress the activity of Lewis acid sites of γ-Al_2O_3 [34, 35]. Moreover, low DME productivity is obtained during one-pot CO_2-hydrogenation over CuZn/ γ-Al_2O_3, where a lot amount of water is formed and low temperature are requested for a thermodynamic

point of view [36-38]. For these reasons, research is focusing on the development of new catalysts with high activity at relatively lower temperature as well as high stability in presence of water. Zeolites are investigating as alternative acid catalysts to γ-Al_2O_3, although physicochemical properties shall be carefully selected. In fact, as reported in recent works, channel system, acidity and crystal morphology of zeolites strongly affect the catalytic behaviour in terms of DME yield, deactivation and coke formation [39-43].

For instance, during methanol dehydration reaction, high coke deposition rate is found for zeolites with 3-dimensional channel system such as MFI, BEA or CHA, while fast deactivation is observed for zeolite with 1-dimensional channel system such as TON, MTW and EUO [39, 41]. On the contrary, FER-type catalyst exhibits high resistance to deactivation and a high inhibiting-features toward coke formation during methanol dehydration reaction. The superiority of FER over the other investigated zeolites was related to its 2-dimensinal channel system with small/medium pore openings that ensure high shape-selectivity towards DME [39]. Moreover, the superiority of FER-type zeolite over γ-Al_2O_3 in terms of resistance in presence of water was recently reported [40].

The utilization of zeolites as acid catalysts for one-pot CO_2/CO hydrogenation was also assessed. The physicochemical properties of zeolites strongly affect the catalytic behaviour of multifunctional catalyst. Even the preparation method of the multifunctional catalyst is of paramount importance. For instance, a superior catalytic performance was demonstrated on hybrid catalysts prepared by oxalate co-precipitation of copper, zinc and zirconium over zeolite crystals respect to conventional mechanical mixture. The generation both of metal-oxides and acid sites in a single grain leads to an increased CO_2 conversion. In particular, when FER-type zeolite is used as dehydration

114 component, higher DME productivity is obtained respect to other zeolites, i.e. MFI and
115 MOR. CuZnZr-FER hybrid catalyst offers a promising DME production via CO_2
116 hydrogenation process thanks to more efficient redox-acid cooperation to convert CO_2
117 into methanol and dehydrate rapidly the alcohol into DME with low production of by-
118 products as carbon monoxide [44-47]. The superiority of FER over other zeolite
119 structures (i.e. TON, MFI, MOR, MTT, FAU) in the syngas-to-DME process was also
120 pointed out by several studies [48-54]. All of this results indicate that the careful choice
121 of the properties of acid catalyst is fundamental for DME production via both tow-step
122 (methanol dehydration) or one-step (syngas/CO_2-to-DME) synthesis way.

123 As extensively reported, the physicochemical properties of zeolites are highly
124 dependent on the synthesis procedure adopted for the synthesis. For instance, the choice
125 of organic structure directing agent (OSDA) is of paramount importance for aluminium
126 distribution, acidic properties and crystals size, being these key parameters for catalysis
127 [55, 56].

128 The present study is devoted to the fine control of the physicochemical properties of
129 FER-type catalysts. The series of samples were synthesised by adopting different
130 synthesis conditions in order to obtain crystals with different acid sites distribution and
131 morphology. Pyrrolidine, ethylenediammine, 1,8-diaminooctane and tetrahydrofuran
132 were used as OSDA. Furthermore, a small addition of sodium lauryl sulphate to the
133 synthesis gel permits to reduce crystal size with no effect on crystallinity.

134 Brønsted/Lewis acid sites distribution and concentration of synthesised materials have
135 been investigated with NH_3-TPD and FT-IR of adsorbed D_3-acetonitrile while crystals
136 morphology has been analysed by scanning electron microscopy. Methanol dehydration
137 to dimethyl ether catalytic tests in the reaction temperature range 180-240 °C, has

permitted to evaluate the catalysts in terms of activity, selectivity, deactivation, and coke formation. The set of experimental data can be used to tailor the properties of FER-type catalysts.

2. EXPERIMENTAL

2.1 Samples preparation

Four different OSDA: pyrrolidine (Py), ethylendiammine (En), tetrahydrofuran (THF) and 1,8-diaminooctane (DAO) were used to synthesise FER samples from a synthesis gel with a Si/Al ratio in the range 8-10. The following chemicals were used in all the synthesis: colloidal silica Ludox AS-40 (SiO_2, 40 wt% suspension in H_2O, Aldrich), sodium aluminate ($NaAlO_2$, Aldrich), aluminium sulphate ($Al_2(SO_4)_3x16H_2O$, Aldrich), sodium hydroxide (pellets, Aldrich), pyrrolidine (Aldrich) ethylenediamine (Fluka), tetrahydrofuran (Aldrich), 1,8-diaminooctane (Aldrich), sodium lauryl sulphate (Aldrich) and distilled water. Synthesis gels were prepared at room temperature, and the crystallization was carried out in stainless-steel Teflon coated autoclave.

Synthesis of FER sample by using pyrrolidine (Py-FER) as OSDA was prepared by adopting the following synthesis gel molar composition [33]:

$$12\ Py - 1.6\ Na_2O - 1\ Al_2O_3 - 20\ SiO_2 - 400\ H_2O$$

In a typical synthesis, sodium aluminate, NaOH and pyrrolidine were dissolved in distilled water and the mixture was stirred until complete dissolution of components. Afterwards, colloidal silica was added dropwise to the solution, and the gel was stirred for 1 hour. The obtained gel transferred in an 80 mL autoclave and left for 30-90 hours at 180 °C in a tumbling oven (rotation speed: 15 rpm).

The effect of a surfactant on crystal morphology of the Py-FER, was evaluated by adding sodium lauryl sulphate (SLS) with an SLS/Al_2 molar ratio equals to 0.3 at the above described synthesis gel, and the obtained sample is labelled as SLS-Py-FER.

Synthesis of FER sample by using ethylendiammine (En-FER) was carried out by adopting the following synthesis gel molar composition [33]:

$$19.7\ En - 1.85\ Na_2O - 15.2\ SiO_2 - 1\ Al_2O_3 - 590\ H_2O$$

Sodium aluminate, NaOH and ethylendiammine were dissolved in distilled, and the mixture was stirred until complete dissolution of components. Afterwards, colloidal silica was added dropwise to the solution, and the gel was stirred for 1 hour. The obtained gel transferred in a 120 mL autoclave and left for 3-12 days in the same conditions of the Py-FER synthesis.

The synthesis of FER sample by using 1,8-diaminooctane as OSDA was performed by a replacing ethylenediamine as it follows:

$$10\ DAO - 1.85\ Na_2O - 15.2\ SiO_2 - 1\ Al_2O_3 - 590\ H_2O$$

NaOH and sodium aluminate were dissolved in distilled water and the mixture was stirred until complete dissolution of components. Afterwards, a DAO in water solution was added and the resulting phase was mixed for 30 minutes. Finally, colloidal silica was added dropwise and the obtained gel was stirred for 1 h prior to transfer it in an autoclave with a volume of 60 mL. Crystallization was performed by adopting the same procedure described for En-FER. More details are reported elsewhere [ref].

The synthesis of FER sample with tetrahydrofuran as OSDA (THF-FER) was performed by adopting the procedure published by Guo et al. [55] with the following synthesis gel molar composition:

$$10\ THF - 4.3\ Na_2O - 20\ SiO_2 - 1\ Al_2O_3 - 400\ H_2O$$

NaOH aqueous solution was added dropwise to a mixture of aluminium sulphate colloidal silica and water. The obtained phase was stirred for 1 h and tetrahydrofuran was added under vigorous stirring. After 1 h, the gel was transferred in an autoclave with a volume of 60 mL and kept at 200 °C for 6-12 days in a static oven [55].

After crystallization, the solid was separated by vacuum filtration and washed several times with distilled water until the pH of filtered solution was close to the neutral value. The obtained white solid was then dried for 15 hours in a static oven kept at 80 °C. In order to remove template from zeolite, air-flow calcination was carried out at 550 °C with an holding time of 8 hours and a heating rate of 2 °C/min. Afterwards, H-form solid was obtained by ion-exchange with a NH_4Cl 1 M solution at 80 °C followed by a secondary air-flow calcination under the same condition of the previous one [56].

2.2 Physicochemical characterization

X-Ray powder diffraction (APD 2000 Pro) (region $5° < 2\theta < 50°$, step 0.02°/ s) was used to verify both purity and crystallinity of obtained phase; the morphology of the crystalline phase was observed on a scanning electron microscope (SEM, FEI model Inspect) and a transmission electron microscopy (TEM, Philips CM12). Atomic absorption spectroscopy (ContraAA® 700 – Analytik Jena) was used for the measurement of content of sodium, aluminum and silicon content in the calcined catalysts.

The specific surface area (by B.E.T. method) and the micropores volume (by *t*-plot method) of the calcined samples were obtained by nitrogen adsorption/desorption isotherms at -196 °C with a ASAP 2020 instrument (Micromeritics).

The ^{27}Al-NMR spectra were acquired on a Bruker Advance 500 MHZ instrument at 130.3 MHz with radiofrequency power of 54 kHz, a pulse length of 4.6 μs with a corresponding angle theta of π/4. Rotors were spun at 14 kHz, and the recycle delay used for both nuclei was 1 second.

Surface acidity of H-form sample was measured by both NH_3-TPD analysis (TPDRO1100, ThermoFisher) and FT-IR analysis by using D_3–acetonitrile as a probe molecule. Detailed procedure is reported elsewhere [57].

2.3 Catalytic tests

Catalytic tests were performed in the temperature range 180 – 240 °C using an experimental apparatus described elsewhere [59, 65]. A mixture of methanol (0.06 mol/mol) and nitrogen as a carrier (60 *N*ml min^{-1}) was fed in a quartz reactor loaded with 70 mg of catalyst in pellets form (300 – 500 μm) fixing the Weight Hourly Space Velocity (WHSV) at 4.5 $gr_{MeOH}\cdot(gr_{cat}\cdot h)^{-1}$. Prior to any test, the catalyst drying was performed under nitrogen flow at 240°C for 3 h.

The product stream composition was determined by a gas chromatograph (Agilent 7890A), equipped with a capillary column (J&W 125–1032) and an FID detector.

Catalyst resistance against deactivation was investigated in Time-On-Stream (TOS) measurements carried out at 240 °C for about 1000 min. The amount of retained carbonaceous species deposited during TOS test was measured by thermo-gravimetric analysis (TGA) in air flow by heating the sample from room temperature to 850 °C (heating rate 5 $°C\cdot min^{-1}$) and attributing the sample weight loss observed between 250 and 700 °C to the deposited carbonaceous species [58].

3. RESULTS AND DISCUSSION

3.1 Structural properties of FER-type zeolites synthesized with different OSDA

X-ray patterns as a function of crystallization time of En-FER, Py-FER, and THF-FER are reported in Figure 1A-C. Crystal growth kinetics of En-FER is relatively slow (see Figure 1A) as traces of FER phase are observed after 3 days and after 6 days the crystalline phase is dominant. A crystallization time of 10 days can be considered as optimal to obtain high crystalline En-FER since, for longer time (12 days), traces of kaetite phase appear. A faster crystal growth kinetic is observed for the system containing pyrrolidine (Py-FER) (see Figure 1B). Although no crystalline phases were observed after 15 hours, the onset of FER-phase crystallization is evident after 30 hours and is completed in the range 60-90 hours. The obtained results are in good agreement with Chen et al. [33], except for some minor differences in terms of crystallization time values that usually arise when different autoclaves volumes are adopted. Furthermore, the addition of sodium lauryl sulphate (SLS-Py-FER) does not affect crystallinity as can be seen in Figure S.1.

Nevertheless, some differences may be noted after 15 h crystallization. In fact, SLS-Py-FER seems to have a higher crystallinity than Py-FER. The presence of surfactant may be responsible of formation of microdroplets that mimic crystallization favouring nucleation [59]. The higher nucleation rate may be responsible of the formation of smaller crystals in SLS-Py-FER sample as later reported.

Guo et al. [55] showed that, for a THF-containing system, crystallization of FER phase occurs in time range 8-12 days, without mentioning any information about the crystallinity evolution over time. Therefore, the crystal growth kinetics of THF-FER was studied and the results are presented in Figure 1C. XRD results show that the THF-containing system yields FER-type phase, but the crystallization time is a key parameter

to be properly chosen, in order to maximise the phase purity. In fact, after 6 days, FER X-Ray peaks appear still with a significant amount of amorphous phase and crystallization time of 8 days can be suggested as optimal value to obtain high crystalline and pure ferrierite (THF-FER sample). Longer crystallization time causes the formation of competitive phases such as MOR and MFI. The formation of MOR phase in this system can be attributed to the higher sodium concentration in the THF-containing synthesis gel (Na/Al=4.3 mol/mol) higher than the previous investigated systems (En-FER, Na/Al=1.85; Py-FER, Na/Al=1.6).

The replacing of En with DAO reduce the induction period as reported in Figure 1-D In fact, in presence of DAO, FER-phase is almost completely crystallized after 3 days whilst only traces of crystalline product is observed when ethylenediamine is used as OSDA.

Figure 2 shows representative SEM micrographs revealing that all samples exhibit the typical of ferrierite plat-like morphology with a well-developed {1 0 0}. However, the crystals differ in size and the level of agglomeration. The En-FER crystals (Figure 2A) have the following characteristics: length 2-3 µm, length/width ratio around 2 and thickness 100 nm, while DAO as OSDA generates smaller crystals with size around 1 µm and lower length/width ratio (around 1.3) as reported in Figure 6D. Py-FER sample shows larger crystals with length 5-6 µm, length/width ratio around 1.6 and thickness 100 nm (Figure 2B). Completely different crystal morphology was observed for THF-FER sample (Figure 2C) where uniform agglomerates of 10-15 µm are observed, as each agglomerate consists of stacked plat-like crystals with thickness around 150 nm. For THF-containing system, it should be reminded that the crystallization is relatively long and the XRD study reveals the presence of other solids (Figure 1.C). Accordingly,

SEM micrographs after 6 and 12 days of crystallization, reported in Figure S.2, confirm the presence of an amorphous phase after 6 days, whilst MFI and MOR phases are clearly present after 12 days. The attribution of crystals to MFI rather MOR phases was carried out referring to SEM analysis reported by Qian et al. [60].

SEM and TEM pictures of SLS-Py-FER sample are reported in Figure 3. They are significantly smaller that the sample synthesised without sodium lauryl sulphate (Figure 6B). The morphology is plate-like and the size below 500 nm. Thus the addition of the surfactant inhibits the growth of the crystals, but retains the high crystallinity of the zeolite (vide supra).

The results of N_2 adsorption analysis are summarized in Table 1. Micropore volume follows the order THF-FER<DAO-FER<Py-FER≈SLS-Py-FER<En-FER. The lower micropore volume values observed for THF-FER and DAO-FER can be related to the higher amount of sodium cations in zeolite channels. Figure S.3 (Supporting Information) highlights the adsorption/desorption isotherms of synthesised samples in protonic form. All of the investigated structure exhibit the pattern of type I isotherm typical of microporous materials [33].

Figure 2 shows the ^{27}Al MAS NMR spectra of the H-form FER-type zeolites obtained in En-, Py-, DAO- and THF-containing systems. They are dominated by a signal centered at around 55 ppm, characteristic of tetra-coordinated aluminium species in zeolite framework. The presence of a second peak at around 62 ppm for Py-FER sample can be associated with tetrahedral aluminium species with a different Al-O-Si bond angle [68]. A relatively weak signal at around 0 ppm revealing the presence of octahedral extra-framework aluminium (below 10%). The observed quadrupolar line

broadening can be caused by distortions of the octahedral symmetry of AlO_6 sites. No octahedral aluminium species were observed on THF-FER sample by NMR analysis.

It is well-known that the zeolite structure is generated by a network of SiO_4 and AlO_4^- tetrahedral linked together by a shared oxygen atom. Due to the presence of trivalent atoms (e.g. aluminium) in the tetrahedral units, the framework offers a negative charge which needs to be balanced with non-framework exchangeable cations that are generally elements of the group IA and group IIA as sodium, potassium, magnesium and calcium [69]. In this work, sodium is used to synthesise FER-type materials, and this is the cation that balances negative charges associated with aluminium atoms. Furthermore, the high quantity of tetrahedral aluminium species detected by NMR analysis, suggests that the Na/Al ratio should be around one. Strikingly, the chemical analysis reported in Table 1 shows that Na/Al is about 0.10 for Py-FER and En-FER, 0.6 for DAO-FER and 0.9 for THF-FER. These results disagree with the previous theoretical assumption, suggesting that sodium cations do not balance an important amount of aluminium species in tetrahedral position. Vuono et al. [67] reported a Na/Al ratio value below to unity (around 0.60) for MCM-49 materials synthesised in the presence of hexamethylenimine despite aluminium was mainly tetra-coordinated as in our case. Forbes et al. [71, 72] report that during the synthesis of ZSM-5/Theta-1 materials in the presence of diethanolammine, the organic molecules were considered to have both a pore-filling role and charge compensatory role. Furthermore, Rollmann et al. [73] assert that protonated amine (e.g. ethylamine, pyrrolidine, hexamethylenimine) play the role as counterion of negative charge associated to tetrahedral aluminium atoms located into zeolite framework, also for FER-type materials. Therefore, because in this work, aluminium atoms are mainly present in tetrahedral coordination, protonated

organic molecules can be reasonably present to compensate negative charge of zeolite lattice. THF-FER exhibits a relative higher Na/Al ratio (around 0.9) showing that AlO_4^- species needs to the presence of sodium cations to be balanced because THF is not able to play a role of counterion [74]. Nevertheless, also for THF-FER, the Na/Al ratio is not equal to one, suggesting the presence of extra-framework aluminium species not detected by the NMR analysis. This aspect will be elucidated during FT-IR results discussion.

3.2 Zeolite acidity

The NH_3-TPD profiles are reported in Figure 9 for all the synthesised samples displaying three main peaks characterised by different ammonia maximum desorption temperatures peaks (T_M) as an indicator of different acid sites family (the higher is T_M, the stronger is the acid sites). No differences in NH_3-TPD profiles can be observed between Py- and SLS-Py-FER (see Figure S. 4), indicating that the presence of surfactant affects crystal morphology rather than acid properties.

As suggested by Niwa and Katada [76, 77], the interpretation of peaks with T_M<300 °C may be quite misleading since the desorption effect may also be related to physically adsorbed ammonia interacting via a hydrogen bond with the NH_4^+ ions adsorbed onto acid sites. In this condition, having comparable desorption energy, the presence of weak acid sites, may be partially hidden by physisorbed ammonia. On the contrary, the peaks with 300°C<T_M<500 °C are associated with ammonia molecules desorbed from strong acid sites (both Brønsted and Lewis acid sites). The peak with T_M>700 °C can be associated to dehydroxylation phenomena [78, 79] since it is detected either in NH_3-

TPD experiments or in the corresponding "blank" TPD experiments performed over the same catalyst and under the same experimental conditions, without NH_3 feed (see Figure S.5 of supplementary information). Weight loss above 700 °C was also detected via TG analysis (Figure S. 6for THF-FER) for the protonic form of the sample reveailing that the dTG peak above 700°C as a dehydroxylation phenomena.

Quantitative results of NH_3-TPD measurements reported in Table 2 indicates how the total acid sites concentration follows the Si/Al ratio on the solid.

Figure 10 depicts the FT-IR spectra of H-ferrierite samples in the OH-stretching region. Two main bands observed at 3745 $cm^{-1}$and 3600 cm^{-1} are associated with terminal silanol Si-OH and Brønsted acid sites Al-OH-Si groups, respectively [80, 81]. A shoulder at around 3645 cm^{-1} is also present. Similar result was reported already [34, 82], but the peak is not well-identified. Peixoto et al. [83] suppose that the observed shoulder can be associated to a silanol group anchored on extra-framework aluminium species (e.g., octahedral aluminium) as reported also by Rachwalik et al. [84] even though in the investigated samples, NMR analysis suggests that octahedral aluminium species are nearly absent. It is known from the literature that aluminium in highly distorted coordination might become NMR silent and the observed band at 3645 cm^{-1} can be associated to OH groups connected to the so called 'invisible' aluminium species [85, 86] that can play a role of Lewis acid sites [87, 88]. The presence of these species could explain the non-stoichiometric Na/Al ratio discussed above.

Curves of Figure 10 indicate that THF-FER sample seems to possess a lower concentration of both terminal silanol Si-OH and Al-OH groups compared with the other samples. Figure S.7 (Supporting Information) reveals that PY-FER and SLS-PY-

FER samples exhibit similar FT-IR spectra in the OH-stretching region except for a slightly lower Si-OH concentration for the surfactant-free sample.

In order to discriminate between Lewis and Brønsted acid sites, deuterated acetonitrile (CD_3CN) was used as a probe molecule following the FT-IR procedure discussed above. FT-IR spectra of adsorbed CD_3CN at different desorption temperatures (ranging between 25°C and 300°C) are reported in Figure 11. The presence of two main bands at about 2296 cm^{-1} and 2322 cm^{-1} reveals the presence of both Brønsted and Lewis acid sites, respectively, in all catalysts. Smaller bands at lower wave length associated with physisorbed acetonitrile are also presents [64]. The concentration of Brønsted and Lewis sites were obtained from the integral intensities of the IR bands of adsorbed CD_3CN at 2296 cm^{-1} and 2322 cm^{-1}, respectively, by using the extinction factor coefficients reported in Section 2. Brønsted and Lewis site distribution of the investigated samples was calculated from the area of bands recorded at 25 °C, and quantitative results in terms of Lewis acid site percentage are summarized in Table 2. Results show that OSDA significantly effects acid sites distribution: the En-FER and DAO-FER exhibit a high Lewis acid sites concentration (around 40%) while the lowest value was 15% of THF-FER. The addition of surfactant did not affect the acid sites distribution as both Py-FER and SLS-Py-FER samples exhibit the same concentration of Lewis acid sites (around 33%). Therefore, considering NH_3-TPD profiles, it is possible to conclude that Py-FER and SLS-Py-FER have a very similar acidity in terms of concentration, distribution, and typology of acid sites, but substantially different crystal size.

In order to estimate the number and the strength of Brønsted and Lewis acid sites the desorption profiles shown in Figure S. 8 were analyzed and the results are reported in

Figure 11. The set of data show that Lewis acid sites are stronger than Brønsted ones for all the samples. The desorption of Brønsted sites becomes significant above 150°C while the Lewis sites are still occupied above 300°C. Only EN-FER sample seems to exhibit slightly weak Lewis acid sites since the desorption of probed molecule starts at a lower temperature. On the contrary, for Brønsted acid sites the acetonitrile molecules desorption starts from 50°C and no occupied sites are present above 250°C. EN-FER, PY-FER and DAO-FER exhibit a similar trend, whilst THF-FER had Brønsted acid sites weaker than the other catalysts. In fact, at 100 °C the 60% of the Brønsted acid sites are desorbed for THF-FER compared with 30% for the other samples.

By considering as strong Lewis acid sites fraction, the value of Lewis acid sites still occupied by CD_3CN molecules at 300 °C, it is possible to calculate the the fraction of Strong Lewis sites reported in (Table 2, last column). The concentration of strong Lewis acid sites follows the order DAO-FER>En-FER>Py-FER (≈SLS-Py-FER)>THF-FER suggesting that synthesis system affect both typology and strength of acid sites. The observed Lewis acid sites can be associated with extra-framework, NMR silent, Al-OH species.

3.4 Catalytic tests

The catalytic activity of synthesised samples was investigated by performing Methanol to dimethyl ether reaction. Figure 13 shows the methanol conversion at different reaction temperatures. The data were calculated as an arithmetic media over three independent measurements during 30 min of Time-On-Stream, always resulting in conversion relative variation below 10%.

The catalytic data show that differences in textural and chemical properties lead to different catalytic activity, except for THF-FER, exhibiting the lowest value of methanol conversion on the investigated reaction conditions. Significant differences in conversion between the samples, excluding THF-FER, which shows substantially lower activity, can be found only at a temperature below 200°C. The lower activity of THF-FER is attributed to the large crystal size, increasing the mass transfer limitation. The effect of crystal size is also evident by comparing Py-FER and SLS-Py-FER that exhibit similar acidity (acid sites concentration and distribution) but different activity. At the reaction temperature of 180°C, methanol conversion on Py-FER is 15% lower than on SLS-Py-FER but the effect tends to disappear when increasing the temperature. DME selectivity data reported in Figure 14 suggest that over both THF-FER and DAO-FER sample only DME is formed at 180 °C whilst a slightly lower selectivity is observed over the others sample. For all the samples, DME selectivity progressively decreases as the reaction temperature increases, and methane, ethylene, propylene and butenes appear in the reaction products.

In order to assess the catalyst stability, the methanol conversion was monitored for about 1000 minutes at 240°C (Figure 15). FER-type catalysts synthesised employing amines as OSDA (En-FER, Py-FER, and DAO-FER), offer high stability in the considered time range. On the contrary, THF-FER shows a progressive deactivation with a conversion drop of about 10% at the end of the test.

The higher deactivation rate observed for THF-FER sample can be attributed to the amount of deposited coke, significantly higher for this sample, as reported in Figure 16. The higher carbon deposit level and the consequent rapid deactivation can be promoted by both largest presences of Brønsted acid sites or by bigger crystal size as both

442 characteristics are present in THF-FER sample. On the contrary, despite the similar
443 acidic properties, the carbon deposit level exhibited by SLS-Py-FER lower than Py-FER
444 can be attributed to nano-sized crystals retarding coke formation [92, 93]. In this
445 direction also goes DAO-FER sample showing a carbon deposit lower that the others
446 micro-sized samples, despite its higher acid sites concentration.

447

448 **4. CONCLUSIONS**

449 FER-type crystals were synthesized employing pyrrolidine (Py) ethylenediamine (En),
450 tetrahydrofuran (THF) as OSDA with the goal to vary the chemical, physical and
451 textural properties of the zeolite. For the first time, 1,8-diaminooctane (DAO) was used
452 as OSDA, and its role in the formation of FER-type structure was studied combining
453 experimental and theoretical methds. A surfactant (sodium lauryl sulphate - SLS) was
454 used in order to tune the crystal size Py-FER and thus nano-sized crystal were
455 synthesized. SLS-obtained nanosized crystals showed similar acidity and improved
456 catalytic activity with respect to the micron-sized Py-FER counterpart. Differences in
457 crystal size and morphology were also found when changing the OSDA, from very
458 large crystals in the case of THF-FER to a typical morphology of ferrierite obtained
459 with amino-containing OSDA. Despite similar Si/Al ration of the initial gels the use of
460 different organic structure directing agents leads to variation of the zeolite framework
461 composition. The OSDA impacts on the Al distribution resulted in catalysts with
462 significant differences in acid sites distribution and strength (Lewis and Brønsted). This
463 result provides new opportunities in tailoring the acid characteristics of FER-type
464 catalysts. This statement is fully supported by the results obtained in the methanol
465 dehydration to DME. Both acidity and crystal size strongly affect the DME selectivity

and reistance towards deactivation. A higher coke amount is deposited on bigger crystals, whilts the utilization of nano-sized crystals strongly retard coke formation. In the light of acidity analysis, one can state that the higher is Lewis acid sites concentrarion the better perfofming is the catalyst for DME production. On the other side the large presence of Brønsted acidy seems to promote the abundant coke formation.

ACKNOWLEDGMENTS

The authors gratefully acknowledge dr. Eddy Dib, Catalysis and Spectroscopy Laboratory LCS ENSICAEN, for NMR analysis and dr. Francesco FRUSTERI, CNR-ITAE "Nicola Giordano" - Messina, for TEM micrographs.

REFERENCES

[1] J. Čeika, A. Krejči, N. Žilková, J. Kitrla, S. Ernst, A. Weber, Microp. Mesopor. Mater. 53 (2002) 121-133.

[2] B. J. Schoeman, E. Babouchkina, S. Mintova, V. P. Valtchev, J. Sterte, J. Porous. Mater. 8 (2001) 13-22.

[3] L. Lakiss, F. Ngoye, C. Can, S. Laforge, Y. Pouilloux, Z. Qin, M. Tarighi, K. Thomas, V. Valtchev, A. Vicente, L. Pinard, J.–P. Gilson, C. Fernandez, J. Catal. 328 (2015) 165-172.

[4] Z. Qin, L. Lakiss, L. Tosheva, J.–P. Gilson, A. Vicente, C. Fernandez, V.Valthcev, Adv. Funct. Mater. 24 (2014) 257-264

[5] M. Guisnet, P. Magnoux, Appl. Catal A: Gen. 54 (1989) 1-27

[6] U. Olsbye, S. Svelle, M. Bjørgen, P. Beato, T.V.W. Janssens, F. Joensen, S. Bordiga, K.P. Lillerud, Angew. Chem. Int. Ed. 51 (2012) 5810-5831.

[7] Z. Zhu, Q. Chen, Z. Xie, W. Yang, C. Li, Microp. Mesopor. Mater. 88 (2006) 16-21.

[8] L.-E. Sandoval-Díaz, J.-A. González-Amaya, C.-A. Trujillo, Microp. Mesopor. Mater. 215 (2015) 229-243.

[9] A. Corma, J. Catal. 216 (2003) 298 – 312.

[10] Y. Gao, B. Zheng, G. Wu, F. Ma, C. Liu, RSC Adv. 6 (2016) 83581-83588.

[11] B. Bonelli, L. Forni, A. Aloise, J. B.Nagy, G. Fornasari, E. Garrone, A. Gedeon, G. Giordano, F. Trifirò, Microp. Mesop. Mater. 101 (2007) 153-160.

[12] L. Forni, G. Fornasari, F. Trifirò, A. Aloise, A. Katovic, G. Giordane, J. B.Nagy, Microp. Mesop. Mater. 101 (2007) 161-168.

[13] B. Wichterlová, N. Žilkova, E. Uvarova, J. Čejka, P. Sarv, C. Paganini, J.A. Lercher, Appl. Catal. A: Gen. 182 (1999) 297-308.

[14] D. Chen, K. Moljord, T. Fuglerud, A. Holmen, Microp. Mesopor. Mater. 29 (1999) 191-203.

[15] F. Di Renzo, Catal. Today 41 (1998) 37-40.

[16] H. Konno, T. Okamura, T. Kawahara, Y. Nakasaka, T. Tago, T. Masuda, Chem. Eng. J. 207 (2012) 490-496.

[17] S. Mintova, J.-P. Gilson, V. Valtchev, Nanoscale 5 (2013) 6693-6703.

[18] J. Pérez-Ramírez, C.H. Christensen, K. Egeblad, C.H. Christensen, J.C. Groen, Chem. Soc. Rev. 37 (2008) 2530-2542.

[19] X. Chen, D. Xi, Q. Sun, N. Wang, Z. Dai, D. Fan, V. Valtchev, Microp. Mesop. Mater. 234 (2016) 401-408.

[20] V. Valtchev, G. Majano, S. Mintova, J. Pérez-Ramírez, Chem. Soc. Rev. 42 (2013) 263-290.

[21] B. Bonelli, L. Forni, A. Aloise, J. B.Nagy, G. Fornasari, E. Garrone, A. Gadeon, G. Giordano, F. Trifirò, Microp. Mesop. Mater. 101 (2007) 153-160.

[22] P. De Luca, D. Violante, D. Vuono, L. Catanzaro, J. B.Nagy, A. Nastro, Microp. Mesop. Mater. 71 (2004) 39-49.

[23] N. Bilba, C.C. Pavel, I. Asaftei, A. Nastro, J. B.Nagy, C. Perry, D. Vuono, P. De Luca, G. Iofsea, Stud. Surf. Sci. Catal. 154 (2004) 334-341.

[24] S. F. Abdo, S. T. Wilson, in: J. Cêjka, R. Morris, P. Nachtigall (Eds.), Zeolites in catalysis: properties and applications, The Royal Society of Chemistry, London, UK, 2017, RSC Catalysis Series 28, pp. 310-350.

[25] X. Chen, T. Todorova, A. Vimont, V. Ruaux, Z. Qin, J.-P. Gilson, V. Valtchev, Microp. Mesop. Mater. 200 (2014) 334-342.

[26] Y. Kamimura, C. Kowenje, K. Yamanaka, K. Itabashi, A. Endo, T. Okubo, Microp. Mesop. Mater. 181 (2013) 154-159.

[27] T.A. Semelsberger, R.L. Borup, H.L. Greene, J. Power Sources 156 (2006) 497 – 511.

[28] S.H. Park, C. S. Lee, Energ. Convers. Manage. 89 (2014) 848 – 863.

[29] T.H. Fleisch, A.Basu, R.A. Sills, J. Nat. Gas Sci. Eng. 9 (2012) 94 – 107.

[30] B.L. Salvi, K.A. Subramanian, N.L. Panwar, Renew. Sust. Energ. Rev. 25 (2013) 404 – 419.

[31] Z. Azizi, M. Rezaeimanesh, T. Tohidian, M. R. Rahimpour, Chem. Eng. Process. 82 (2014) 150 – 172.

[32] P. Haro, F. Trippe, R. Stahl, E. Henrich, Appl. Energ. 108 (2013) 54-65.

[33] D. Chen, K. Moljord, A. Holmen, Microp. Mesop. Mater. 164 (2012) 239-250.

[34] E. Catizzone, G. Bonura, M. Migliori, F. Frusteri, G. Giordano, Molecules, 23 (2018) 31-58.

[35] M. Xu, J. H. Lunsford, D. W. Goodman, A. Bhattacharyya, Appl. Catal. A: Gen. 149 (1997) 289-301.

[36] S. P. Naik, T. Ryu, V. Bui, J. D. Miller, N. B. Drinnan, W. Zmierczak, Chem. Eng. J. 167 (2011) 362 – 368.

[37] J. Ereña, R. Garoña, J. M. Arandes, A. T. Aguayo, J. Bilbao, Int. J. Chem. React. Eng. 3 (2005).

[38] M. De Falco, M. Capocelli, G. Centi, Chem. Eng. J. 294 (2016) 400-409

[39] E. Catizzone, A. Aloise, M. Migliori, G. Giordano, Microp. Mesop. Mater. 243 (2017) 102-111.

[40] E. Catizzone, M. Milgiori, A. Purita, G. Giordano, J. Energ. Chem. 30 (2019) 162-169

[41] E. Catizzone, Z. Cirelli, A. Aloise, P. Lanzafame, M. Migliori, G. Giordano, Catal. Today 304 (2018) 39-50.

[42] E. Catizzone, S. Van Daele, M. Bianco, A. Di Michele, A. Aloise, M. Migliori, V. Valtchev, G. Giordano, Appl. Catal. B: Env. 243 (2019) 273-282.

[43] M. Migliori, E. Catizzone, A. Aloise, G. Bonura, L. Gómez-Hortigüela, L. Frusteri, C. Cannilla, F. Frusteri, G. Giordano, J. Ind. Eng. Chem. 68 (2018) 196-208.

[44] G. Bonura, M. Migliori, L. Frusteri, C. Cannilla, E. Catizzone, G. Giordano, F. Frusteri, J. CO_2 Util. 24 (2018) 398-406.

[45] F. Frusteri, G. Bonura, C. Cannilla, G. Drago Ferrante, A. Aloise, E. Catizzone, M. Migliori, G. Giordano, Appl. Catal. B: Env. 176 (2015) 522-531.

[46] G. Bonura, F. Frusteri, C. Cannilla, G. Drago Ferrante, A. Aloise, E. Catizzone, M. Migliori, G. Giordano, Catal. Today 277 (2016) 48-54.

[47] G. Bonura, C. Cannilla, L. Frusteri, A. Mezzapica, F. Frusteri, Catal. Today 281 (2017) 337-334.

[48] S.-H. Kang, J. W. Bae, K.-W. Jun, H. S. Potdar, Catal. Comm. 9 (2008) 2035-2039.

[49] J. W. Jung, Y. J. Lee, S. H. Um, P. J. Yoo, D. H. Lee, K.-W. Jun, J. W. Bae, Appl. Catal. B: Env. 126 (2012) 1-8.

[50] J. W. Bae, S.-H. Kang, Y.-J. Lee, K.-W. Jun, Appl. Catal. B: Env. 90 (2009) 426-435.

[51] J. H. Flores, D. P. B. Peixoto, L. G. Appel, R. R. de Avillez, M. I. Pais da Silva, Catal. Today 172 (2011) 218-225.

[52] Q. Xe, P. Chen, P. Peng, S. Liu, P. Peng, B. Zhang, Y. Cheng, Y. Wan, Y. Liu, R. Ruan, RSC Adv. 5 (2015) 26301-26307.

[53] P. S. S. Prasad, J. W. Bae, S.-H. Kang, Y.-J. Lee, K.-W. Jun, Fuel Process. Technol. 89 (2008) 1281-1286.

[54] R. Montesano, A. Narvaez, D. Chadwick, Appl. Catal. A: Gen. 482 (2014) 69-77.

[55] G. Guo, Y. Sun, Y. Long, Chem. Comm. 19 (2000) 1893-1894

[56] M. Migliori, A. Aloise, G. Giordano, Catal. Today 227 (2014) 138-143.

[57] P. Lanzafame, G. Papanikolaou, S. Perathoner, G. Centi, M. Migliori, E. Catizzone, G. Giordano, Appl. Catal. A: Gen. 580 (2019) 186-196.

[58] E. Catizzone, A. Aloise, M. Migliori, G. Giordano, Appl. Catal. A: Gen. 502 (2015) 215-220.

[59] R. K. Ahedi, A. N. Kotasthane, B. S. Rao, A. Manna, B. D. Kulkarni, J. Coll. Inter. Sci. 236 (2001) 47-51.

[60] B. Qian, G. Guo, X. Wang, Y. Zeng, Y. Sun, Y. Long, Phys. Chem. Chem. Phys. 3 (2001) 4164-4169.

TABLES CAPTIONS

Table 1 Chemical composition, pore volume and surfaces characteristics of synthesised FER-type materials.

Table 2 Acidic properties of investigated catalysts.

Table 3 Calculated binding energies and lengths for the investigated SDA-FER systems from DFT simulation

FIGURES CAPTIONS

Figure 1 XRD pattern of FER samples synthesized with the following templates: (A) ethylendiammine, (*****) indicates the presence of Kaetite phase; (B) pyrrolidine; (C) tetrahydrofuran, (▼) and (♦) denote the presence of MOR and MFI phase, respectively; (D) 1,8-diaminooctane (DAO).

Figure 2 SEM micrographs of FER-type materials synthesised with En (A), Py (B), THF (C) and DAO (D).

Figure 3 SEM (left) and TEM (right) micrographs of FER-type materials synthesised by adding SLS to a Py-containing system.

Figure 4 ^{27}Al MAS NMR spectra of the H-forms of ferrierite synthesized with En (a), Py (b), THF (c) and DAO (d).

Figure 5 NH_3-TPD profiles of En-FER (a), Py-FER (b), THF-FER (c) and DAO-FER (d).

Figure 6 FT-IR spectra of OH groups of En-FER (a), Py-FER (b), THF-FER (c) and DAO-FER (d) after evacuation at 300 °C for 4h.

Figure 7 Fraction of Brønsted (●) and Lewis (■) acid sites free of adsorbed D_3CN molecules as a function of desorption temperature; En-FER (A), Py-FER(B), THF-FER(C) and DAO-FER(D).

Figure 8 Methanol conversion as a function of reaction temperature over the investigated samples; WHSV= 4.5 h^{-1}.

Figure 9 DME selectivity as a function of reaction temperature over the investigated samples; WHSV= 4.5 h^{-1}.

Figure 10 Methanol conversion versus Time on Stream observed at 240 °C and WHSV= 4.5 h^{-1}.

Figure 11 Carbon deposit over the investigated sample after 1000 min of TOS at 240 °C and WHSV= 4.5 h^{-1}.

SAMPLE	***Na/Al_{bulk} [a]*** ***[mol/mol]***	***Si/Al_{bulk} [a]*** ***[mol/mol]***	***S_{BET} [b]*** ***[m^2/g]***	***V_{mic} [c]*** ***[cm^3/g]***
Py-FER	*0.1*	*8.4*	*329*	*0.131*
En-FER	*0.1*	*7.4*	*306*	*0.140*
THF-FER	*0.9*	*7.7*	*280*	*0.115*
DAO-FER	*0.6*	*6.6*	*287*	*0.125*
SLS-Py-FER	*0.1*	*8.4*	*340*	*0.133*

[a] Atomic absorption

[b] BET superficial area

[c] Micropore volume calculated by *t*-plot method

Table 1

SAMPLE	*NH_3-uptake* *[µmol/g_{cat}]*	*$T_{M,LT}$[a]* *[°C]*	*x_{LT}[b]*	*$T_{M,HT}$[c]* *[°C]*	*x_{HT}[d]*	*Lewis acid sites[e]* *[%]*	*Strong Lewis acid sites[f]* *[%]*
Py-FER	*965*	*232*	*0.35*	*454*	*0.65*	*0.34*	*0.14*
En-FER	*1052*	*245*	*0.30*	*436*	*0.70*	*0.41*	*0.16*
THF-FER	*929*	*236*	*0.31*	*474*	*0.69*	*0.15*	*0.10*
DAO-FER	*1418*	*231*	*0.40*	*455*	*0.60*	*0.40*	*0.24*
SLS-Py-FER	*965*	*235*	*0.33*	*458*	*0.67*	*0.32*	*0.13*

[a] Temperature of maximum desorption of NH_3 between 100 and 300°C

[b] Fractional population of sites between 100 and 300°C

[c] Temperature of maximum desorption of NH_3 above 300°C

[d] Fractional population of sites above 300°C

[e] Estimated by FT-IR analysis of adsorbed D_3-acetonitrile at 25°C

[f] Estimated by FT-IR analysis of adsorbed D_3-acetonitrile at 300°C

Table 2

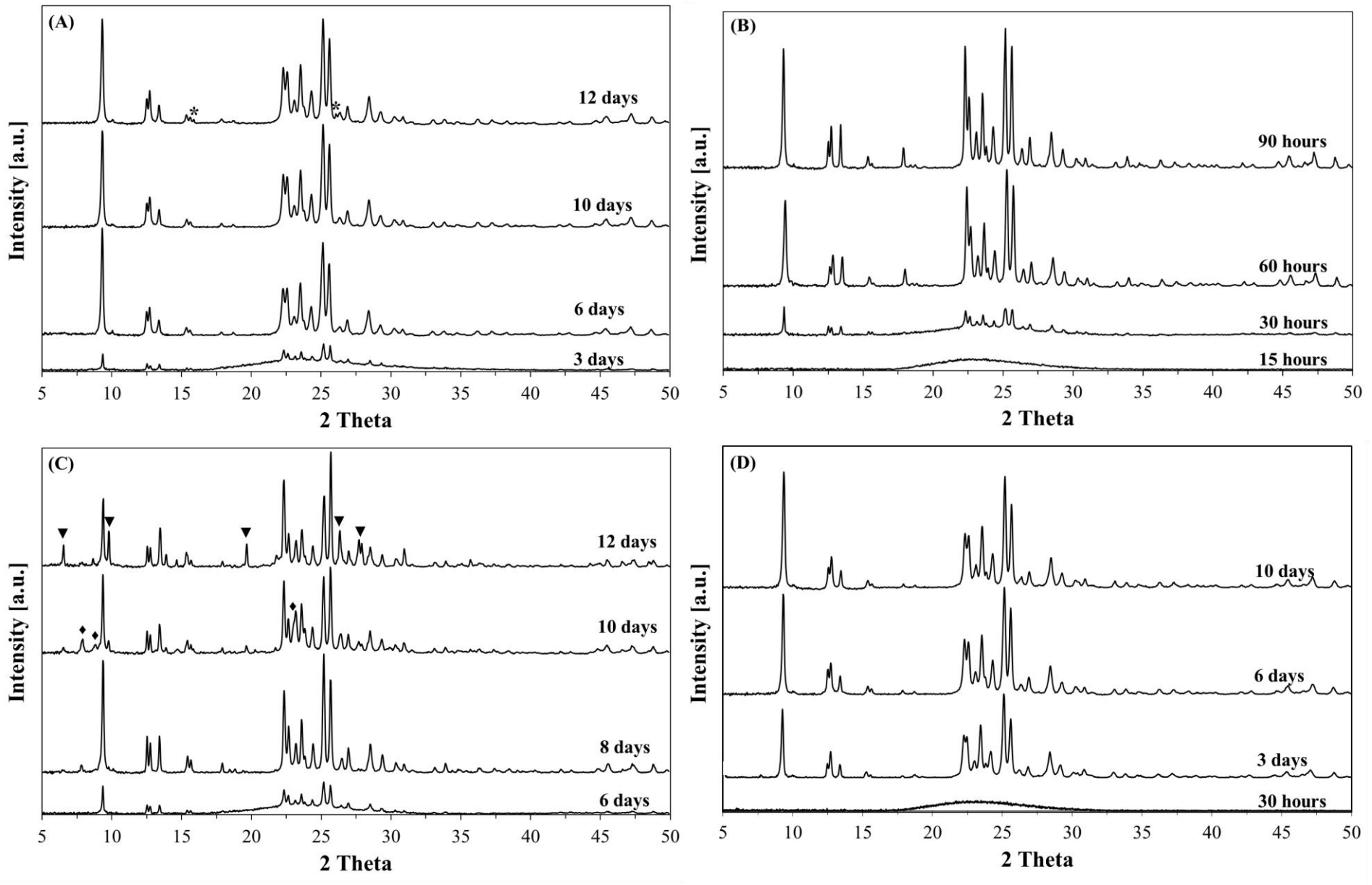
(A)
12 days
10 days
6 days
3 days
Intensity [a.u.]
2 Theta
(B)
90 hours
60 hours
30 hours
15 hours
Intensity [a.u.]
2 Theta
(C)
12 days
10 days
8 days
6 days
Intensity [a.u.]
2 Theta
(D)
10 days
6 days
3 days
30 hours
Intensity [a.u.]
2 Theta

Figure 1

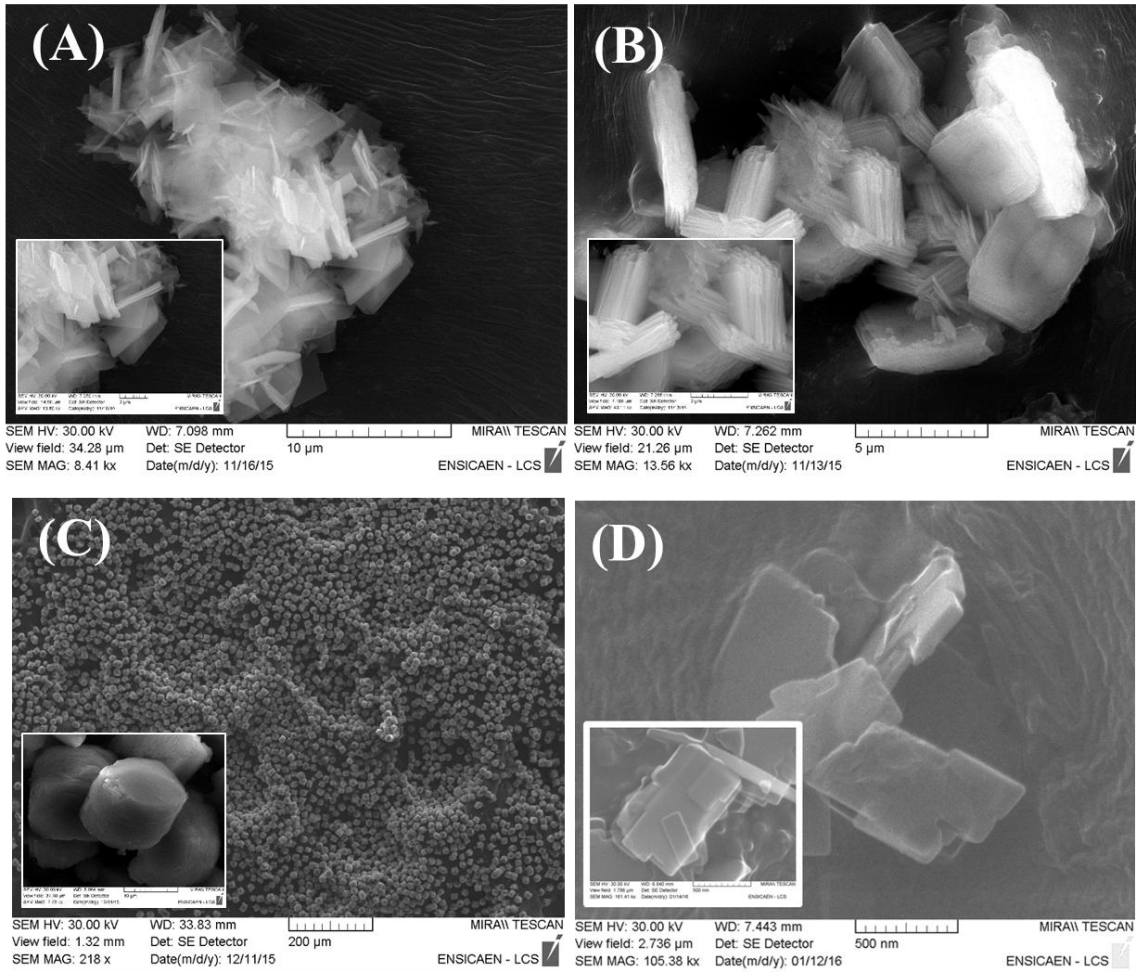
(A)
SEM HV: 30.00 kV
WD: 7.098 mm
MIRA\\ TESCAN
View field: 34.28 µm
Det: SE Detector
10 µm
SEM MAG: 8.41 kx
Date(m/d/y): 11/16/15
ENSICAEN - LCS
(B)
SEM HV: 30.00 kV
WD: 7.262 mm
MIRA\\ TESCAN
View field: 21.26 µm
Det: SE Detector
5 µm
SEM MAG: 13.56 kx
Date(m/d/y): 11/13/15
ENSICAEN - LCS
(C)
SEM HV: 30.00 kV
WD: 33.83 mm
MIRA\\ TESCAN
View field: 1.32 mm
Det: SE Detector
200 µm
SEM MAG: 218 x
Date(m/d/y): 12/11/15
ENSICAEN - LCS
(D)
SEM HV: 30.00 kV
WD: 7.443 mm
MIRA\\ TESCAN
View field: 2.736 µm
Det: SE Detector
500 nm
SEM MAG: 105.38 kx
Date(m/d/y): 01/12/16
ENSICAEN - LCS

Figure 2

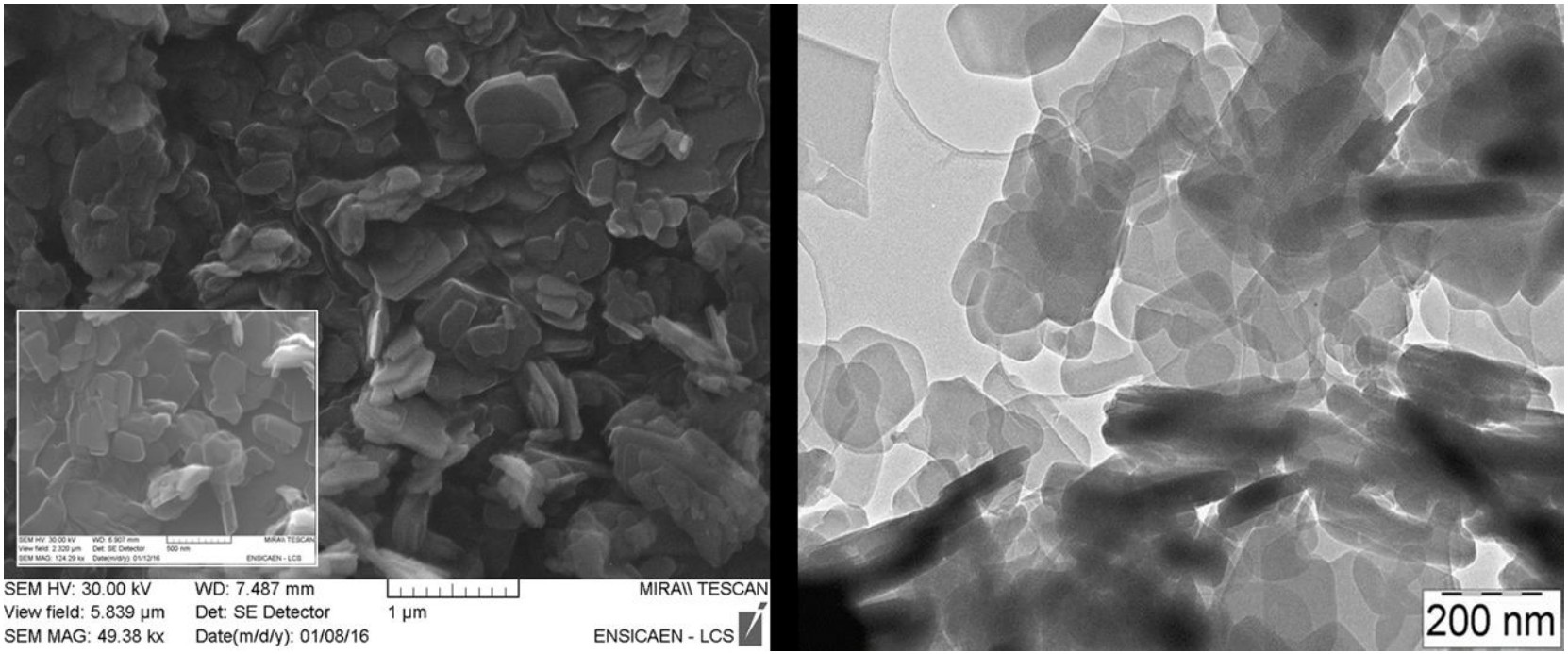
SEM HV: 30.00 kV
WD: 7.487 mm
MIRA\\ TESCAN
View field: 5.839 µm
Det: SE Detector
1 µm
SEM MAG: 49.38 kx
Date(m/d/y): 01/08/16
ENSICAEN - LCS
200 nm

Figure 3

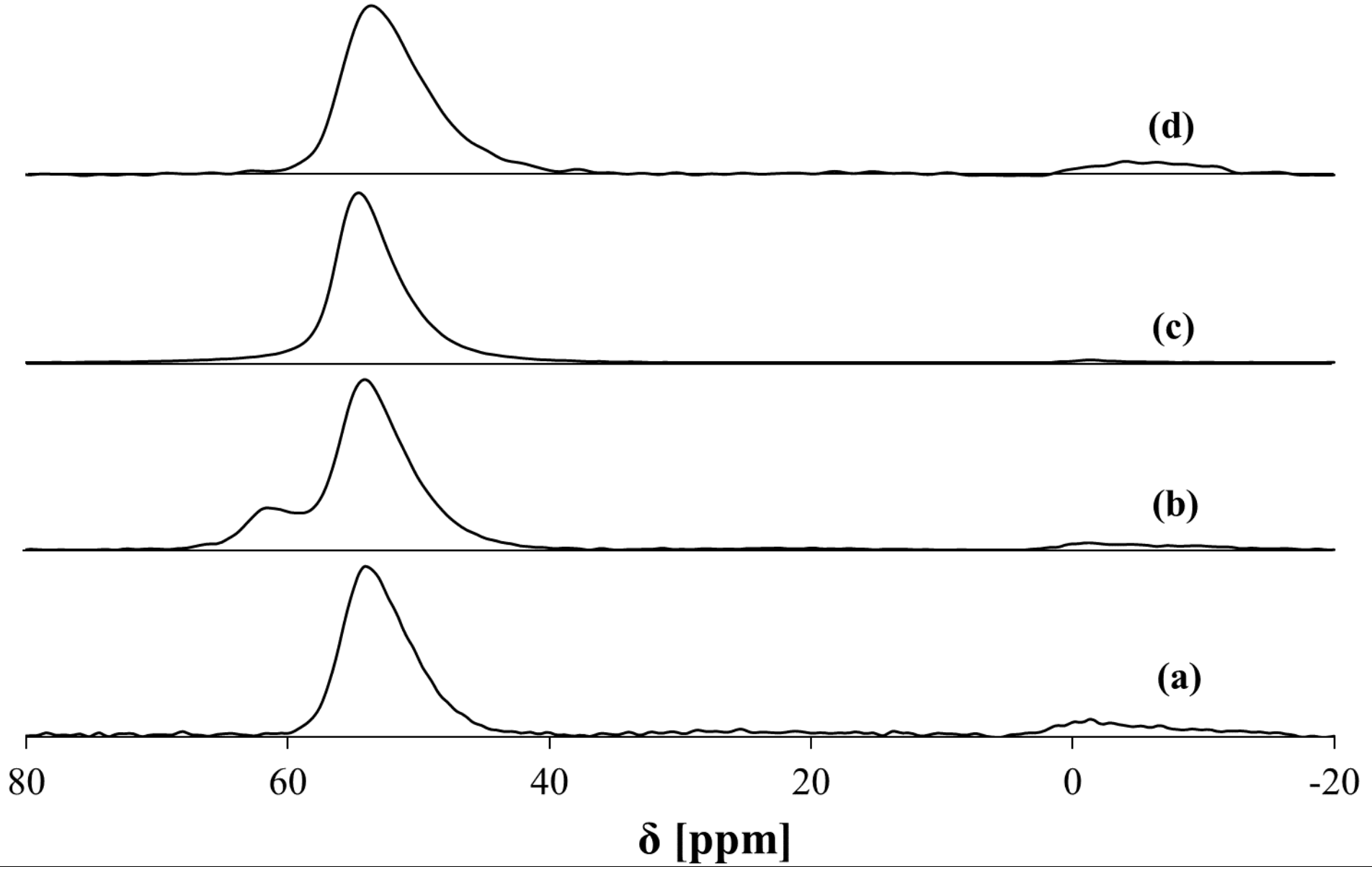

Figure 4

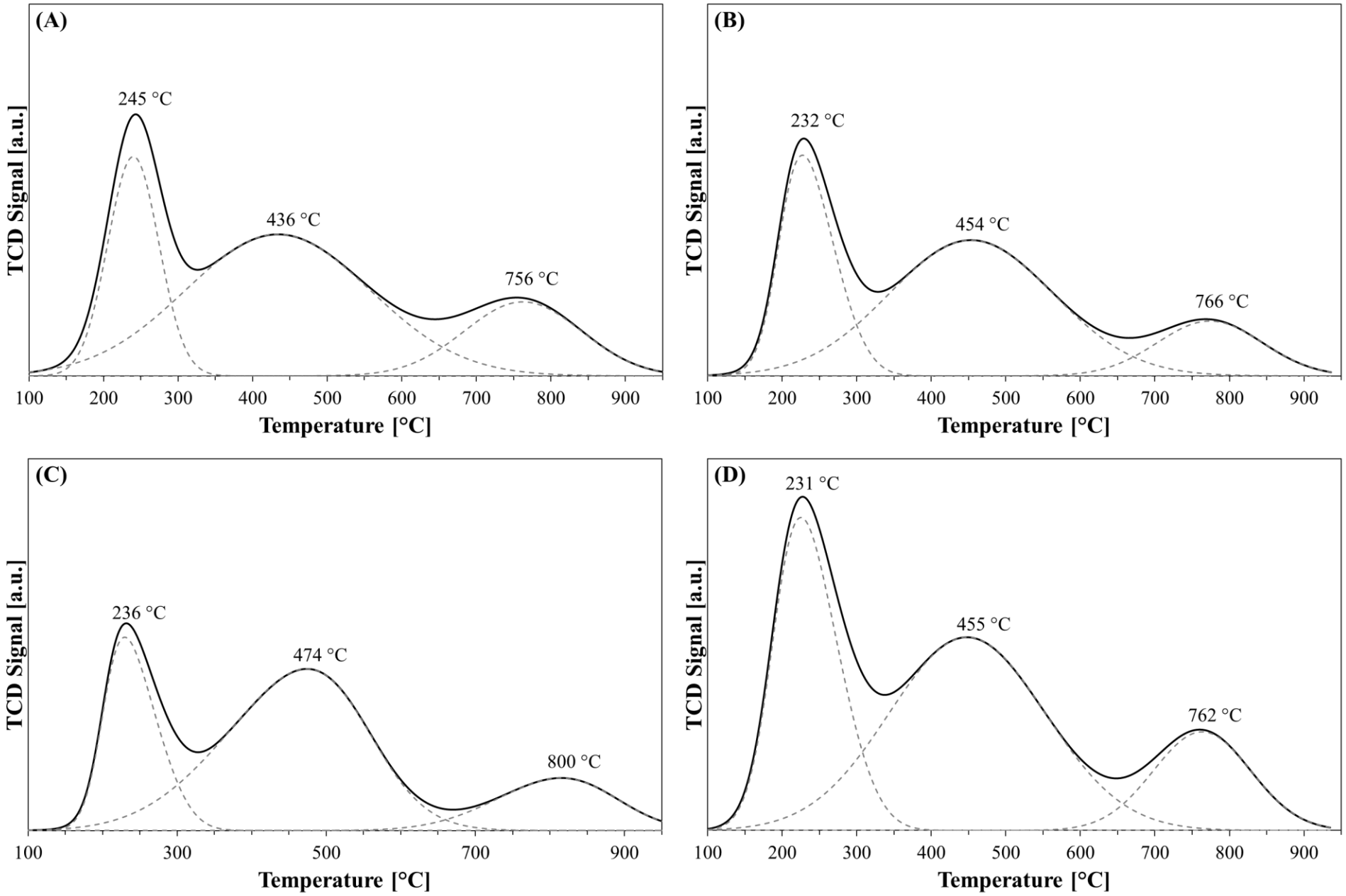
(A)
245 °C
436 °C
756 °C
TCD Signal [a.u.]
Temperature [°C]
(B)
232 °C
454 °C
766 °C
TCD Signal [a.u.]
Temperature [°C]
(C)
236 °C
474 °C
800 °C
TCD Signal [a.u.]
Temperature [°C]
(D)
231 °C
455 °C
762 °C
TCD Signal [a.u.]
Temperature [°C]

Figure 5

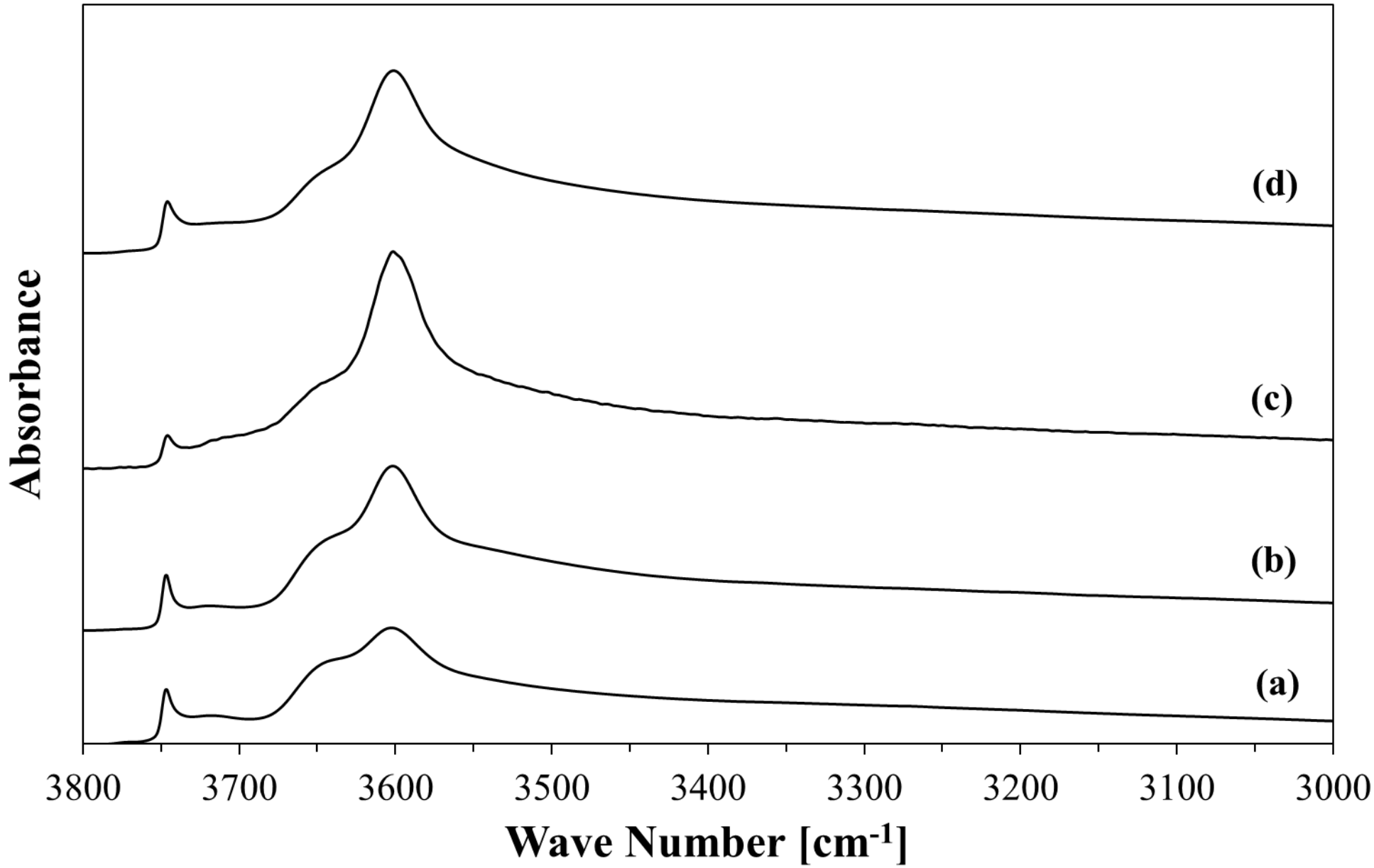
Absorbance
(d)
(c)
(b)
(a)
3800
3700
3600
3500
3400
3300
3200
3100
3000
Wave Number [cm-1]

Figure 6

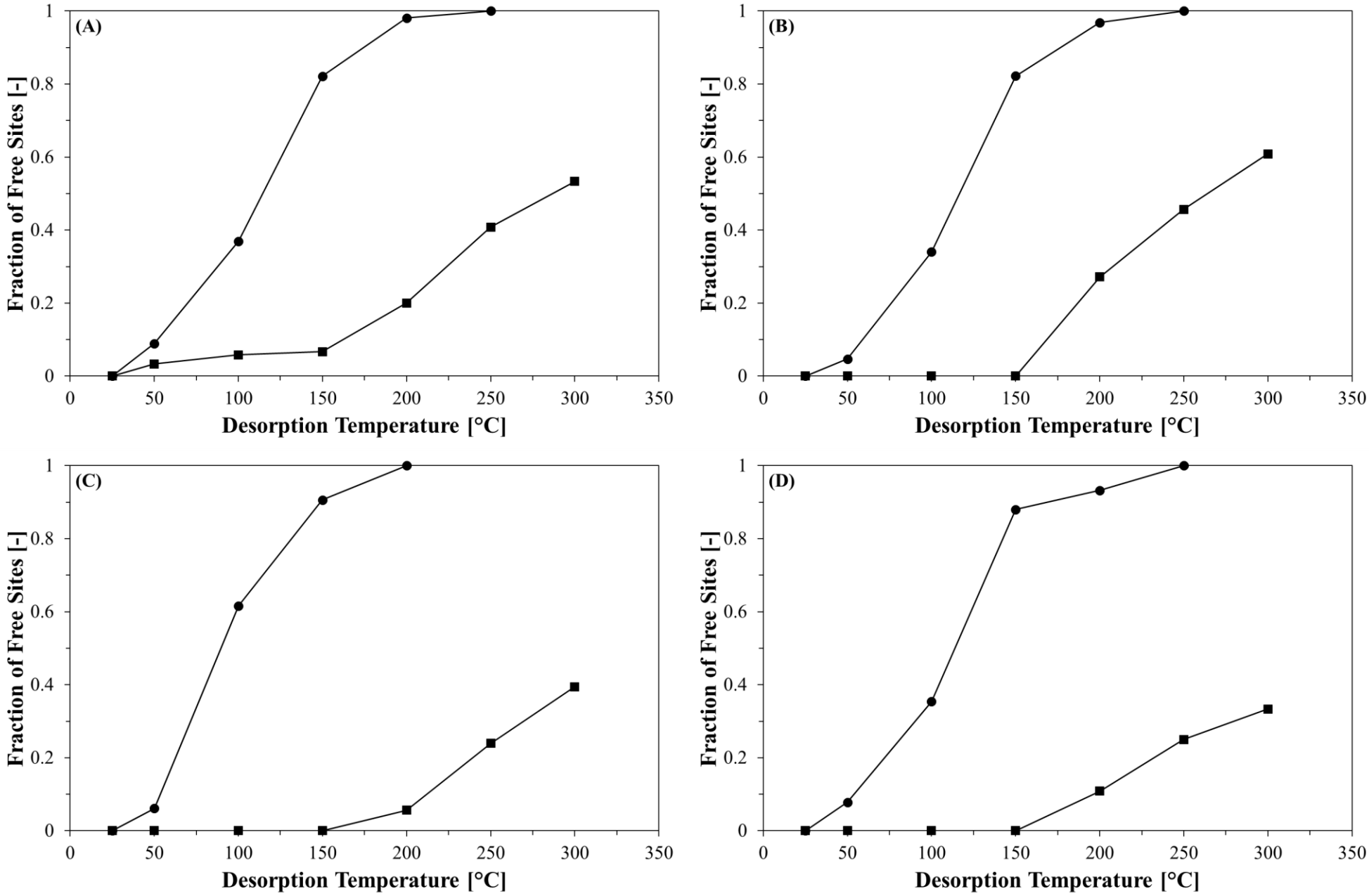
(A)
(B)
(C)
(D)
Fraction of Free Sites [-]
Desorption Temperature [°C]
0
0.2
0.4
0.6
0.8
1
0
50
100
150
200
250
300
350

Figure 7

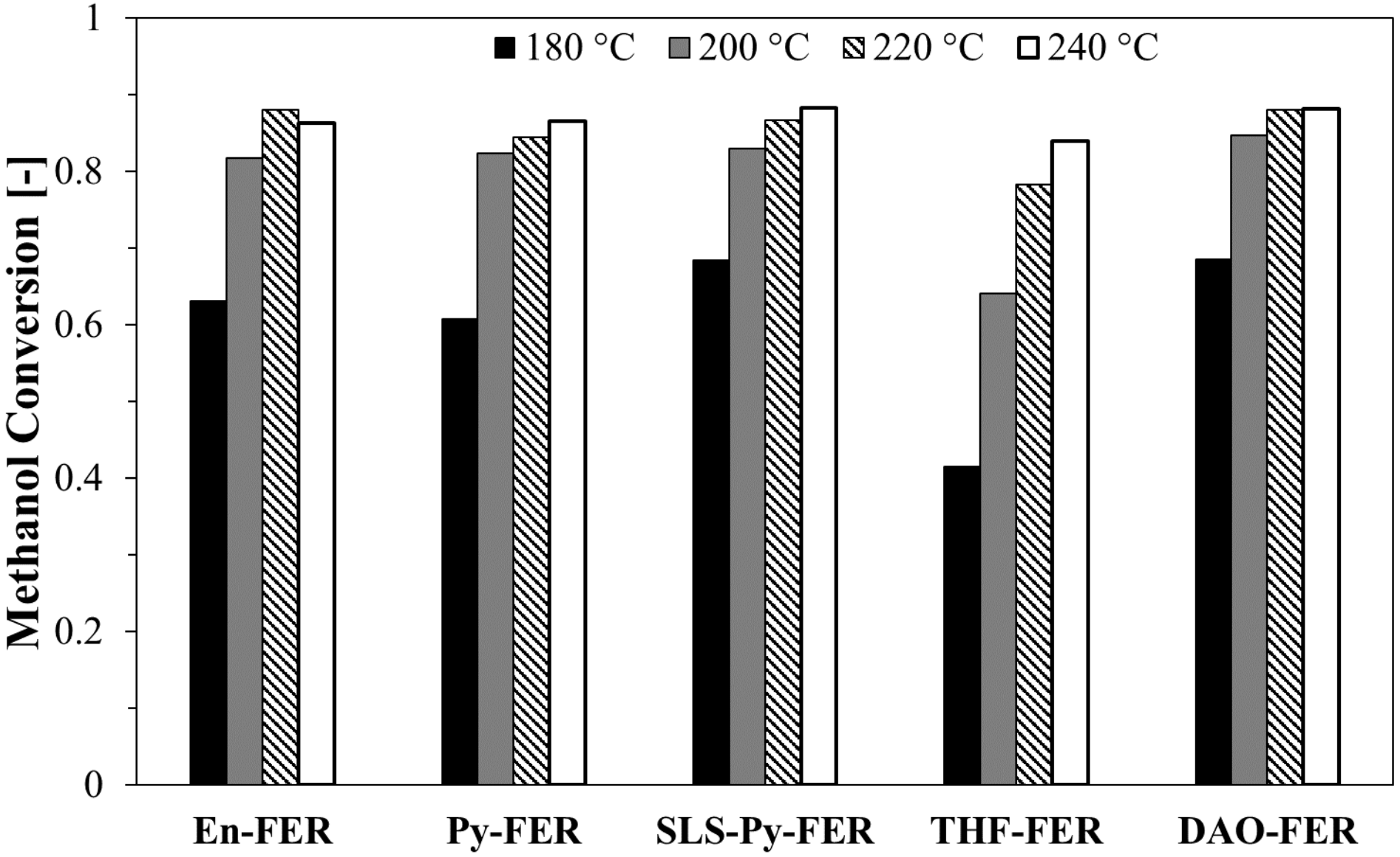
180 °C
200 °C
220 °C
240 °C
Methanol Conversion [-]
1
0.8
0.6
0.4
0.2
0
En-FER
Py-FER
SLS-Py-FER
THF-FER
DAO-FER

Figure 8

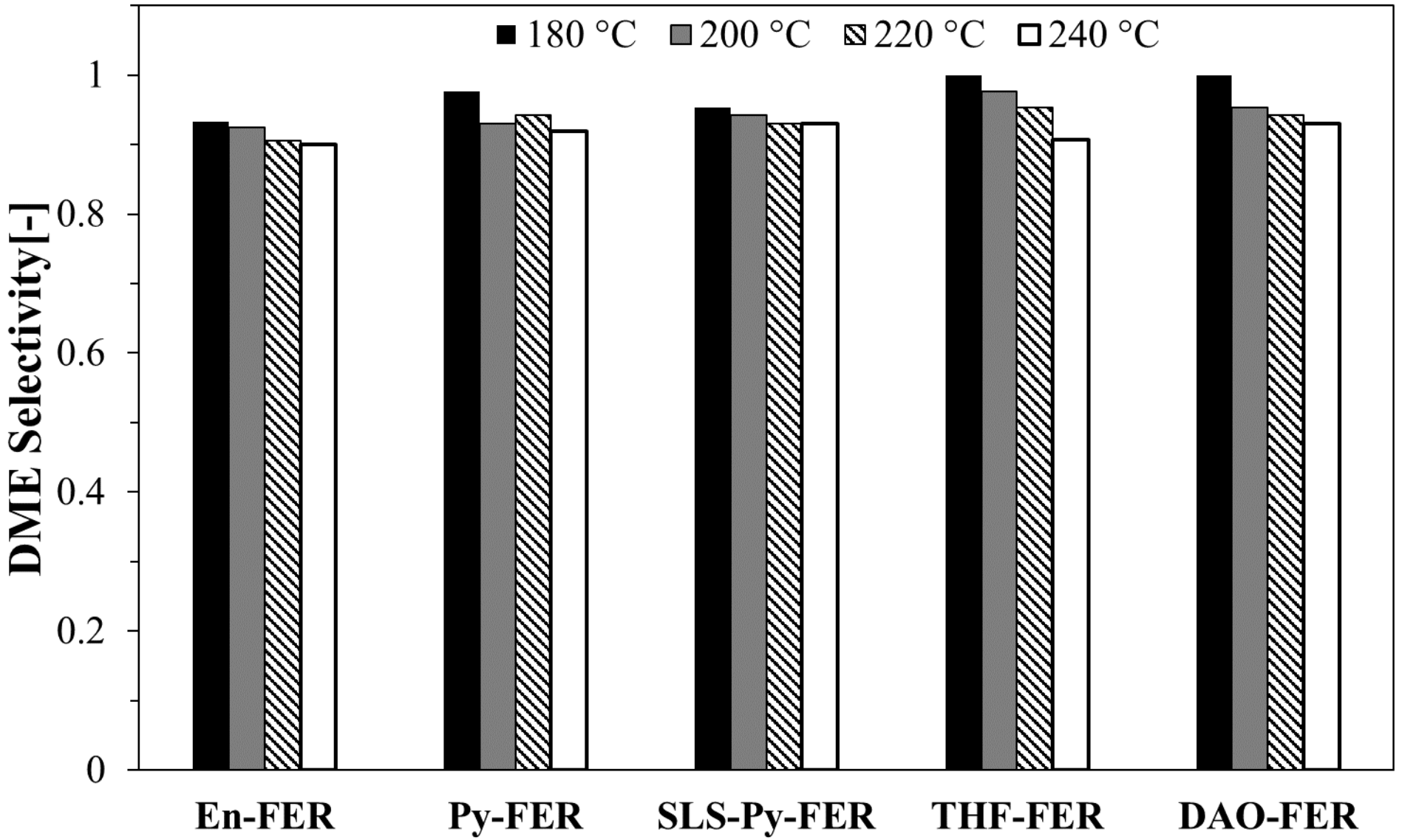
180 °C
200 °C
220 °C
240 °C
DME Selectivity[-]
1
0.8
0.6
0.4
0.2
0
En-FER
Py-FER
SLS-Py-FER
THF-FER
DAO-FER

Figure 9

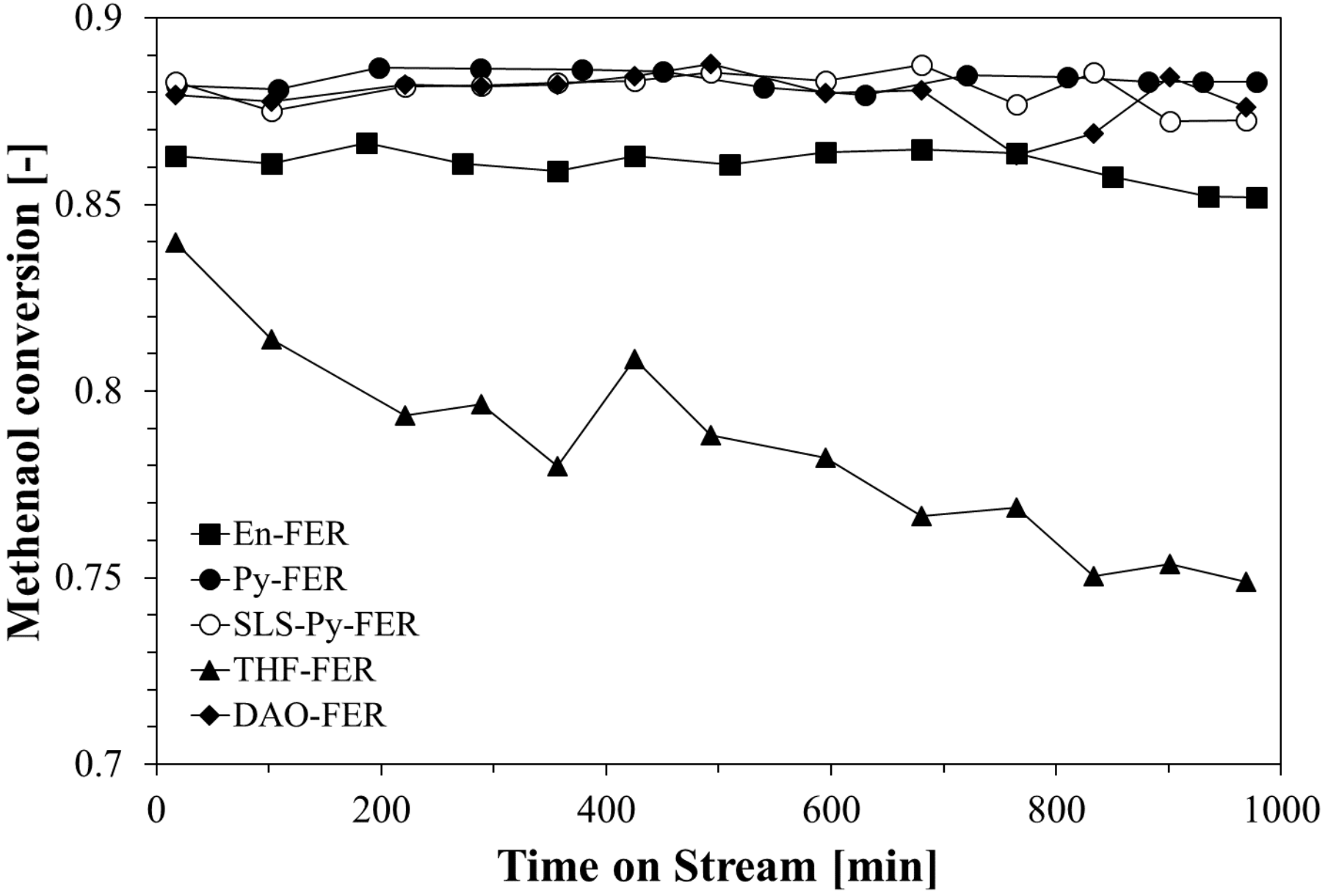
0.9
0.85
0.8
0.75
0.7
Methenaol conversion [-]
0
200
400
600
800
1000
Time on Stream [min]
En-FER
Py-FER
SLS-Py-FER
THF-FER
DAO-FER

Figure 10

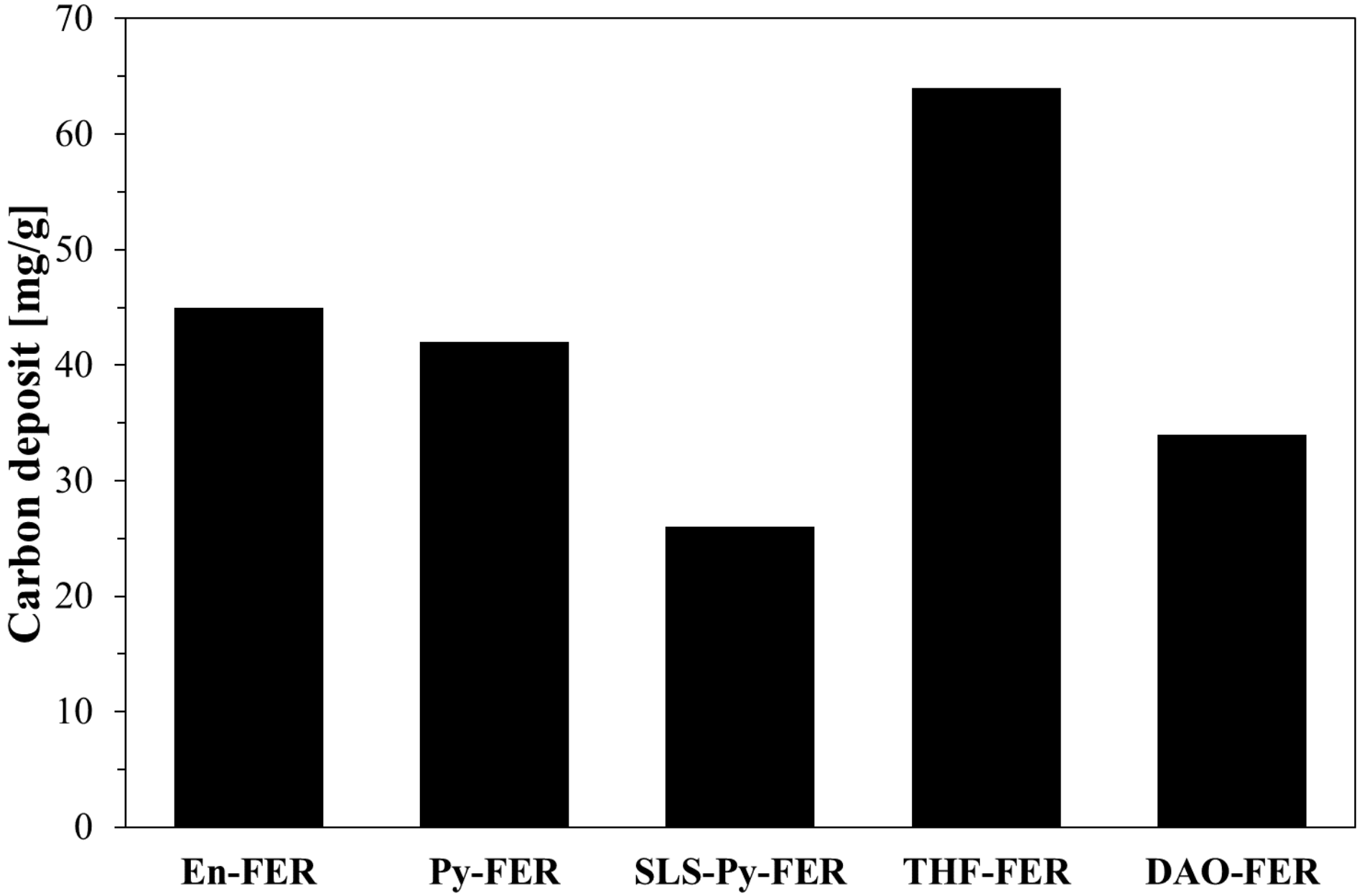
Carbon deposit [mg/g]
70
60
50
40
30
20
10
0
En-FER
Py-FER
SLS-Py-FER
THF-FER
DAO-FER

Figure 11